STRUCTURAL CHEMISTRY

ISSN 2053-2296

Synthesis, crystal structure and *in-silico* evaluation of arylsulfonamide Schiff bases for potential activity against colon cancer

Sherif O. Kolade,[a,b] Oluwafemi S. Aina,[a] Allen T. Gordon,[b] Eric C. Hosten,[b] Idris A. Olasupo,[a] Adeniyi S. Ogunlaja,[b]* Olayinka T. Asekun[a] and Oluwole B. Familoni[a]*

[a]Department of Chemistry, University of Lagos, Akoka-Yaba, Lagos, Nigeria, and [b]Department of Chemistry, Nelson Mandela University, Port Elizabeth 6031, South Africa. *Correspondence e-mail: adeniyi.ogunlaja@mandela.ac.za, familonio@unilag.edu.ng

Received 5 December 2023
Accepted 11 March 2024

Edited by A. Lemmerer, University of the Witwatersrand, South Africa

This article is part of a collection of articles to commemorate the founding of the African Crystallographic Association and the 75th anniversary of the IUCr.

Keywords: Schiff base; arylsulfonamide; colon cancer; crystal structure; molecular docking; ADMET.

CCDC reference: 2305610

Supporting information: this article has supporting information at journals.iucr.org/c

This report presents a comprehensive investigation into the synthesis and characterization of Schiff base compounds derived from benzenesulfonamide. The synthesis process, involved the reaction between *N*-cycloamino-2-sulfanilamide and various substituted *o*-salicylaldehydes, resulted in a set of compounds that were subjected to rigorous characterization using advanced spectral techniques, including ^{1}H NMR, ^{13}C NMR and FT–IR spectroscopy, and single-crystal X-ray diffraction. Furthermore, an in-depth assessment of the synthesized compounds was conducted through Absorption, Distribution, Metabolism, Excretion and Toxicity (ADMET) analysis, in conjunction with docking studies, to elucidate their pharmacokinetic profiles and potential. Impressively, the ADMET analysis showcased encouraging drug-likeness properties of the newly synthesized Schiff bases. These computational findings were substantiated by molecular properties derived from density functional theory (DFT) calculations using the B3LYP/6-31G* method within the Jaguar Module of Schrödinger 2023-2 from *Maestro* (Schrodinger LLC, New York, USA). The exploration of frontier molecular orbitals (HOMO and LUMO) enabled the computation of global reactivity descriptors (GRDs), encompassing charge separation (E_{gap}) and global softness (S). Notably, within this analysis, one Schiff base, namely, 4-bromo-2-{*N*-[2-(pyrrolidine-1-sulfonyl)phenyl]carboximidoyl}phenol, **20**, emerged with the smallest charge separation (ΔE_{gap} = 3.5780 eV), signifying heightened potential for biological properties. Conversely, 4-bromo-2-{*N*-[2-(piperidine-1-sulfonyl)phenyl]carboximidoyl}phenol, **17**, exhibited the largest charge separation (ΔE_{gap} = 4.9242 eV), implying a relatively lower propensity for biological activity. Moreover, the synthesized Schiff bases displayed remarkeable inhibition of tankyrase poly(ADP-ribose) polymerase enzymes, integral in colon cancer, surpassing the efficacy of a standard drug used for the same purpose. Additionally, their bioavailability scores aligned closely with established medications such as trifluridine and 5-fluorouracil. The exploration of molecular electrostatic potential through colour mapping delved into the electronic behaviour and reactivity tendencies intrinsic to this diverse range of molecules.

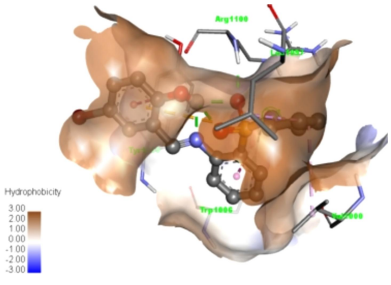

1. Introduction

The quest for effective anticancer agents remains a pivotal challenge in medicinal chemistry and pharmacology, particularly in the context of colon cancer, which is among the leading causes of cancer-related mortality worldwide (Kumar *et al.*, 2023*a*,*b*). The synthesis of novel compounds and the exploration of their biological activities are critical steps in the development of new therapeutic agents. In this connection, arylsulfonamide Schiff bases have emerged as a class of compounds with significant potential due to their versatile

chemical structures and promising pharmacological profiles (Irfan *et al.*, 2020; Muhammad-Ali *et al.*, 2023; Dueke-Eze *et al.*, 2020).

Schiff bases, characterized by their imine functional group (–C═N–), have been studied extensively for their diverse pharmacological activities, including anticancer properties (Alblewi *et al.*, 2023). The introduction of an arylsulfonamide moiety into Schiff base structures has been hypothesized to enhance their biological activity, owing to the known efficacy of the sulfonamide group in various therapeutic agents (Abd El-Wahab *et al.*, 2020; Elsamra *et al.*, 2022). The rationale behind this hypothesis centres on exploring the anticancer potential of Schiff bases, particularly focusing on their interaction with colon cancer. Extensive literature has already underscored their efficacy as anticancer agents (Abd-Elzaher *et al.*, 2016). Remarkably, Schiff bases have demonstrated activity against colon cancer and have been documented for such effects (Matela, 2020). Notably, the combination of benzenesulfonamide with a Schiff base has been reported, merging the bioactive attributes of sulfonamides and Schiff bases to investigate potential synergies between these well-established functional groups (Afsan *et al.*, 2020). The cumulative evidence of their enhanced activity spurred our interest in undertaking the present study.

Tankyrase poly(ADP-ribose) polymerase, a crucial enzyme involved in DNA repair and the regulation of various cellular processes, has been implicated in the development of colon cancer (Feng & Koh, 2013; Eisemann & Pascal, 2020). Tankyrase's involvement in Wingless-related integration site (Wnt) signaling, which governs cell growth, motility and differentiation, makes it a significant target (Pai *et al.*, 2017). Colorectal cancer, a prevalent form of cancer worldwide, often arises from precancerous polyps in the colon or rectum. Tankyrase's modification of Axin through poly(ADP-ribose) chains disrupts the Axin complex, leading to Axin degradation and β-catenin stabilization. The accumulation of β-catenin contributes to the progression of colon cancer (Gao *et al.*, 2014). Under normal circumstances, Axin aids in regulating the Wnt pathway by facilitating β-catenin degradation (Huang & He, 2008). However, mutations in colon cancer can lead to the persistent accumulation of β-catenin, even in the absence of Wnt signaling, promoting uncontrolled cell growth and tumour formation (Behrens, 2000). Inhibiting specific amino acid residues in human tankyrase poly(ADP-ribose) polymerase using Schiff bases, such as (*E*)-2-[(2-hydroxybenzylidene)amino]benzenesulfonamide derivatives (**17**–**23**) (Fig. 1), could potentially prevent the accumulation of β-catenin, holding promise for effective intervention (Meyer *et al.*, 2006).

Our research also delves into the crystal structure of benzenesulfonamides (Kolade *et al.*, 2020), which, along with our exploration of the crystal structure of a Schiff base sulfonamide, forms a comprehensive investigation into the potential therapeutic avenues these compounds may offer.

2. Experimental

2.1. Instruments and measurements

All reagents were purchased from Millipore Sigma (Germany and South Africa) and were used without further purification. The melting points were determined on an electrothermal digital melting-point apparatus and are uncorrected. Reactions were monitored by thin-layer chromatography (TLC) on Merck silica gel 60 F254 precoated plates using a dichloromethane/*n*-hexane (2 or 1.4:1 *v*/*v*) solvent system visualized under a UV lamp (254 nm). Column chromatography was performed with silica gel (70–230 mesh ASTM) and mobile phases were as indicated. Sample crystallization was achieved by the slow evaporation of the indicated solvent systems at ambient temperature. IR spectra were obtained using a Bruker Tensor 27 platinum ATR–FT–IR spectrometer. The ATR–FT–IR spectra were acquired in a single mode with a resolution of 4 cm^{-1} over 32 scans in the region 4000–650 cm^{-1}. ^1H and ^{13}C NMR spectra were recorded in $CDCl_3$ on a Bruker 400 MHz spectrometer. Chemical shift values were measured in parts per million (ppm) downfield from

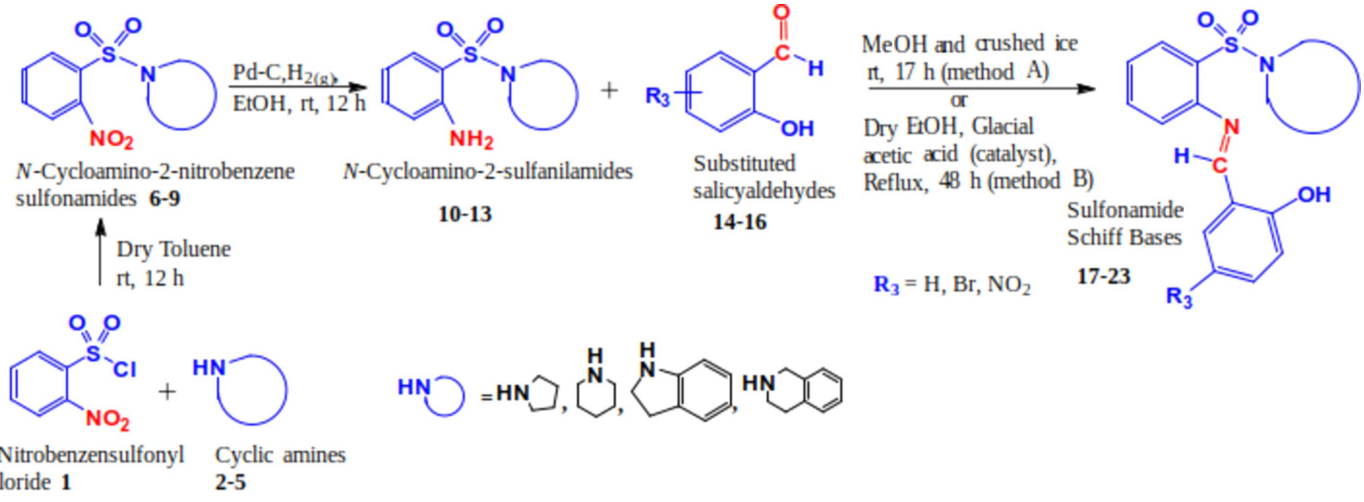

Figure 1
General reaction scheme of the formation of potentially bioactive sulfonamide Schiff bases.

Table 1
Experimental details for **18**.

Crystal data	
Chemical formula	$C_{18}H_{19}BrN_2O_3S$
M_r	423.32
Crystal system, space group	Orthorhombic, *Pbca*
Temperature (K)	296
a, *b*, *c* (Å)	12.4070 (9), 17.4250 (14), 17.5276 (12)
V (Å^3)	3789.3 (5)
Z	8
Radiation type	Mo *Kα*
μ (mm^{-1})	2.30
Crystal size (mm)	0.84 × 0.43 × 0.12
Data collection	
Diffractometer	Bruker APEXII CCD
Absorption correction	Multi-scan (*SADABS*; Bruker, 2016)
T_{min}, T_{max}	0.133, 0.241
No. of measured, independent and observed [$I > 2\sigma(I)$] reflections	27860, 3356, 2255
R_{int}	0.060
(sin $\theta/\lambda)_{max}$ (Å^{-1})	0.597
Refinement	
$R[F^2 > 2\sigma(F^2)]$, $wR(F^2)$, *S*	0.062, 0.172, 1.09
No. of reflections	3356
No. of parameters	227
H-atom treatment	H-atom parameters constrained
$\Delta\rho_{max}$, $\Delta\rho_{min}$ (e Å^{-3})	0.52, −0.38

Computer programs: *APEX2* (Bruker, 2016), *SAINT* (Bruker, 2016), *SHELXT2018* (Sheldrick, 2015*a*), *SHELXL2018* (Sheldrick, 2015*b*), *ShelXle* (Hübschle *et al.*, 2011), *ORTEP-3 for Windows* (Farrugia, 2012), *PLATON* (Spek, 2020) and *Mercury* (Macrae *et al.*, 2020).

tetramethylsilane (TMS), and coupling constants (*J*) are reported in Hertz (Hz). Theoretical studies were performed for the compounds and, in each case, their single-crystal X-ray diffraction (SC-XRD) structures were used for optimization and global reactivity descriptor (GRD) calculations.

2.2. Synthesis and crystallization

2.2.1. Synthesis of sulfonamide Schiff bases. The general reaction scheme for the formation of potentially bioactive sulfonamide Schiff bases is shown in Fig. 1. The *N*-cycloamino-2-sulfanilamides were prepared as reported previously (Kolade *et al.*, 2022) by reacting the aminosulfanilamides with substituted *o*-salicylaldehyde either at room temperature or under reflux to obtain the required Schiff bases in good yields (57–80%). Only *o*-salicylaldehyde and *N*-piperidinyl-2-sulfanilamide gave the required Schiff base at room temperature, and the others were refluxed to give the required products.

2.2.1.1. Method A: synthesis of N^1-(2^1-hydroxybenzylidenyl)-N-piperidinyl-2-sulfanilamide ***17***. *N*-Piperidinyl-2-sulfanilamide **11** (0.100 g, 0.417 mmol) was dissolved in methanol (5 ml) and 2-hydroxybenzaldehyde, or *o*-salicylaldehyde, **14** (0.056 g, 0.05 ml, 0.459 mmol), was added dropwise to the solution with stirring. Crushed ice (1.00 g) was added to the stirring mixture after 5 min. The reaction mixture was stirred at ambient temperature for 17 h and monitored with TLC. On completion, the mixture was filtered, using a Buckner funnel, and the residue was air-dried, dissolved in warm methanol and filtered hot to leave single crystals of **17** on slow evaporation. The physical properties and the spectroscopic data are presented in the supporting information.

2.2.1.2. Method B: synthesis of N^1-(5^1-bromo/nitro-2^1-hydroxybenzylidenyl)-N-cycloamino-2-sulfanilamides ***18–23***. To a stirring solution of *N*-cycloamino-2-sulfanilamides **10–13** (1.0 mmol) in ethanol (10 ml) was added 5-bromo(nitro)-*o*-salicylaldehydes **15–16** (1.3 mmol), followed by glacial acetic acid (10 drops) as catalyst. The whole mixture was refluxed for 48 h and monitored with TLC. After completion, the reaction mixture was allowed to cool to ambient temperature and kept in the fume hood for 24 h. The residue was then recrystallized from ethanol (10 ml) and filtered hot to leave crystals of **18–23** on slow evaporation. The physical properties and the spectroscopic data are presented in the supporting information.

2.3. Docking studies

2.3.1. Selection of reference drugs and cancer protein macromolecule. Common anticancer standard drugs, such as capecitabine (ID: 60953), 5-fluorouracil (ID: 3385) and trifluridine (ID: 6256), were downloaded from *Pubchem* (https://pubchem.ncbi.nlm.nih.gov/, last accessed on May 25, 2023) and saved in .sdf format as reference to compare inhibitory performance with the synthesized chemical compounds. In order to evaluate the lead compounds as inhibitors of the tankyrase poly(ADP-ribose) polymerase family responsible for cancer pathogenesis (Shirai *et al.* 2020), its protein crystal structure (PDB entry 6kro) was downloaded from www.rcsb.org (last accessed on April 20, 2023).

2.3.2. Preparation of ligands, reference drugs and protein molecules for docking. Synthesized compounds (drawn using *Chemdraw* 14.0 and saved in .sdf format) and the selected reference drugs saved as .sdf files were opened in PyRx 0.8 *Autodock Vina* software (Kondapuram *et al.*, 2021). Energy minimization was carried out, followed by conversion into protein databank partial charge (pdbqt) ligands. The crystal structure of the protein molecule tankyrase poly(ADP-ribose) polymerase at a resolution of 1.90 Å was also uploaded into *BIOVIA Discovery Studio* (Dassault Systémes, 2020). The binding sites were determined and all unwanted heteroatoms and water molecules were removed, while polar hydrogen bonds were added to give pure protein and saved as .pdb files (Pawar & Rohane, 2021).

2.3.3. Molecular docking. Docking simulations were performed with PyRx *AutoDock* using the Lamarkian genetic algorithm and default procedures for docking a flexible ligand to a rigid protein. Blind docking was initially performed to identify all potential binding sites on the target protein within a 90 × 75 × 75 cubic grid centre. A grid spacing of 1.00 Å was used for the calculation of the grid maps using the autogrid module of *AutoDock* tools. For each ligand, a set of nine independent runs were performed for the enzyme run against all ligands and reference drugs. Clear identification of the potential binding sites is followed by docking of ligands to the sites and the most probable and energetically favourable binding conformations were determined (Trott & Olson, 2010). Docking solutions were analyzed and ranked on the

Table 2
Hydrogen-bond geometry for **18** (Å, °).

Cg is the centroid of the C11–C16 ring.

D—H···*A*	*D*—H	H···*A*	*D*···*A*	*D*—H···*A*
O1—H1*A*···N1	0.82	1.86	2.586 (5)	146
C1—H1···O2^{i}	0.93	2.54	3.363 (6)	149
C16—H16···O2^{i}	0.93	2.64	3.461 (6)	147
C23—H23···O3	0.93	2.43	2.846 (7)	107
C25—H25···O3^{ii}	0.93	2.49	3.220 (6)	135
C26—H26···O1^{i}	0.93	2.62	3.467 (7)	151
C35—H35*B*···O2	0.97	2.43	2.852 (7)	106
C32—H32*B*···*Cg*^{iii}	0.97	2.88	3.664 (7)	139

Symmetry codes: (i) $x+\frac{1}{2}, y, -z+\frac{1}{2}$; (ii) $x+\frac{1}{2}, -y+\frac{1}{2}, -z$; (iii) $-x+\frac{3}{2}, y-\frac{1}{2}, z$.

basis of the *Vina* scoring functions. All calculations were carried out on PC-based machines running Microsoft Windows 10 operating systems. The resulting structures were visualized and analyzed using the *Discovery Studio* visualizer.

2.4. Refinement

Crystal data, data collection and structure refinement details are summarized in Table 1. Carbon-bound H atoms were added in idealized geometrical positions in a riding model. Nitrogen-bound H atoms were located in a difference map and refined freely. The H atom of the hydroxy group was allowed to rotate with a fixed angle around the C—O bond to best fit the experimental electron density. The Hirshfeld surface analyses were performed with *CrystalExplorer* (Version 21.5; Spackman *et al.*, 2021).

3. Results and discussion

3.1. Chemistry

N^1-(5^1-Substituted-2^1-hydroxybenzylidenyl)-*N*-cycloamino-2-sulfanilamides **17**–**23** were prepared from the reaction of *N*-cycloamino-2-sulfanilamides **10**–**13** [as reported previously by Kolade *et al.* (2022)] with substituted *o*-salicylaldehyde either at room temperature or under reflux to obtain the required Schiff bases in good yields (57–80%). Only *o*-salicylaldehyde and *N*-piperidinyl-2-sulfanilamide gave the required Schiff base at room temperature, and the others were refluxed to obtain the desired products. The N^1-(2^1-hydroxybenzylidenyl)-*N*-piperidinyl-2-sulfanilamide **17**, which was prepared at room temperature (Method A), was aimed at establishing an eco-friendly protocol. The reaction progress was monitored by TLC.

All the compounds synthesized were characterized by their melting points and their IR, ^{1}H/^{13}C NMR and MS spectra. In order to clarify the mode of bonding on the ligands, their IR spectra (as presented in the supporting information) confirm the formation of the sulfonamide Schiff base ligands **17**–**23** by the appearance of a strong absorption band at around 1614–1618 cm^{-1}, which is attributed to stretching vibrations of the azomethine group and the absence of the original aldehydic bond (–C═O) and NH_2 vibrations (Salehi *et al.*, 2019). The stretching vibrations of aromatic carbon-to-carbon double bonds (C═C) of the compounds are observed at 1512–1570 cm^{-1}, while the strong absorption bands which appeared at around 1300–1331 and 1119–1155 cm^{-1} are indexed to $(S{=}O)_2$ asymmetric and symmetric stretching frequencies, respectively. The IR spectra provided in the supporting information also reveal other diagnostic bands that further corroborate the formation of Schiff base ligands.

The ^{1}H NMR spectra (see supporting information) of sulfonamide Schiff bases (ligands) **17**–**23** were recorded in $CDCl_3$, using tetramethylsilane (TMS) as the internal standard. The signals at 1.36–4.46 ppm in the ^{1}H NMR spectra of the ligands result from the protons of the methylene groups (–C**H**$_2$–). The singlet signals which correspond to the imine groups (–C**H**═N–) in these ligands are observed at 8.12–8.67 ppm. The phenolic protons (–OH), the most deshielded protons, are clearly indicated at 12.31–13.50 ppm. The deshielded nature of the phenolic OH hydrogen is likely a consequence of it forming a strong resonance-assisted intramolecular O—H···N hydrogen bond. The aromatic protons of the compounds are recorded in the range 6.66–8.44 ppm. Finally, the success of the formation of the sulfonamide Schiff bases is corroborated by the ^{13}C NMR spectra (see supporting information) of compounds **17**–**23**, which show the azomethine C atoms (–**C**═N–) at the chemical environments of 160–162 ppm, while the most deshielded phenolic C atoms occur at 163–166 ppm and the aromatic C atoms are observed at 111–148 ppm.

3.2. Crystal structure

Compound **18** formed pale-yellow platelets with the orthorhombic space group *Pbca* (Table 1). The close *ortho* positioning of the two functional groups on the central arene ring forces their rotation, with a resulting dihedral angle of 30.8 (2)° for the least-squares planes through the piperidine and the iminomethylphenol groups, and dihedral angles of 77.17 (17) and 51.82 (12)°, respectively, with the central linking arene group. The iminomethylphenol group is planar, with an intramolecular O—H···N interaction of 1.86 Å, forming a ring closure that can be described with an *S*(6) graph-set descriptor (Table 2). The intermolecular hydrogen-bond interactions are dominated by the O atoms from the sulfonyl group, with a number of C—H···O═S interactions, resulting in three chains of interactions having *C*(7), *C*(9) and *C*(7) descriptors. The Hirshfeld surface illustrated in Fig. S1 (see supporting information) clearly shows these interactions. The hydroxy group also contributes and is involved in a C—H···O interaction of 2.54 Å, resulting in a *C*(8) chain interaction. The presence of these C—H···O interactions is indicated on the Hirshfeld surface fingerprint plot as H···O (see Fig. S2). There is also an intermolecular C—H···π(ring) interaction of 2.88 Å to the centroid of the C11–C16 ring. This interaction is indicated by H···C on the Hirshfeld surface fingerprint plot (Fig. S2). Table S3 (see supporting information) lists the percentage reciprocal hydrogen surface contact areas, with the H···H interactions having the largest percentage contact. The closest H···H contact indicated in Fig. S2 arises between H atoms on the arene rings between two ad-

jacent iminomethylphenol groups. The H···O/O···H and H···C/C···H interactions have similar contact surface areas, while H···Br/Br···H interactions are also present.

3.3. Theoretical calculations

3.3.1. DFT calculations. Molecular orbital calculations, encompassing full geometry optimization, were methodically conducted on the Schiff base derivatives alongside the established pharmaceutical compounds trifluridine, capecitabine and 5-fluorouracil. These sophisticated calculations were executed using the Jaguar module within *Maestro* (Version 13.6.122) and *MMshare* (Version 6.2.122, Release 2023-2). This involved the integration of the basis set 6-31G* level, harmonized with the hybrid density functional theory (DFT) that incorporates the Becke 3-parameter exchange potential (Becke, 1993; Prokopenko *et al.*, 2019; Jędrzejczyk *et al.*, 2022; Pandi *et al.*, 2022). This intricate approach paved the way for the meticulous determination of crucial molecular properties. The focus of this investigation involved the precise computation of the highest occupied molecular orbital (HOMO) and the lowest unoccupied molecular orbital (LUMO) using the aforementioned methodology. The outcomes of these meticulous calculations, which illuminate the intricate electronic structure and reactivity of the molecules, served as the foundation for the subsequent computation of pivotal global reactivity descriptors. These encompass a spectrum of descriptors, notably the ionization potential (I), electron affinity (A), chemical potential (μ), electronegativity (χ), global hardness (η), global softness (S) and global electrophilicity (ω) values (Gordon *et al.*, 2022).

3.3.2. Global reactivity descriptors of the synthesized Schiff bases and standard drugs. Density functional theory (DFT) stands as a widely embraced technique for *ab-initio* assessments of diverse molecular components. Among its manifold utilities, it holds prominence in discerning the characteristics of frontier molecular orbitals (FMOs), a pivotal factor in elucidating various reaction types and predicting the most reactive sites within conjugated systems (da Silva *et al.*, 2006). This comprehension of structure–property relationships assumes paramount importance in the endeavour to craft enhanced pharmaceutical agents, given that the molecular configuration profoundly influences the performance of drugs (Mahmood *et al.*, 2022).

The bedrock for global vital reactivity descriptors lies in the FMO properties, precisely, the HOMO and LUMO energy values. Through a judicious application of DFT energetics, this study delved into the intricate tapestry of three-dimensional electronic states intrinsic to the molecules under scrutiny. As such, the analysis offered an unprecedented glimpse into the transferability of lone pairs, the nuances of bond interactions, and the reactivity landscape within the specific molecular milieu (Hall *et al.*, 2009). In its totality, this exhaustive computational inquiry provides an illuminating vista into the intricate electronic characteristics and reactivity proclivities of the molecules under examination. The insights gleaned from this study significantly enrich our understanding of their potential roles and behaviours across a spectrum of chemical scenarios.

In the present context, the compounds under scrutiny underwent a meticulous exploration of their quantum chemical attributes. Specifically, the focus was on the localization energies of the HOMO and the LUMO. These energies, encapsulated within the rubric of FMOs, serve as linchpins in upholding chemical stability. Moreover, they emerge as potent tools for dissecting donor–acceptor interactions. The HOMO embodies a molecule's capacity to donate an electron, while the LUMO signifies its propensity to accept an electron. A lower LUMO value indicates an augmented inclination for electron acceptance, while higher HOMO values delineate a heightened disposition to donate electrons to unoccupied molecular orbitals (Yele *et al.*, 2021). Considering the context of the LUMO within the synthesized Schiff bases, **19** displays the most intriguing attribute, featuring the lowest energy level for the LUMO orbital (−2.4963 eV), indicative of its pronounced tendency to accept electrons. Conversely, **17** showcases the highest LUMO energy level (−1.3287 eV). This establishes an order of increasing electron-accepting tendency among the compounds: **19** > **20** > **23** > **21** > **18** > **22** > **23** > capecitabine > trifluridine > **17** > 5-fluorouracil (Table 3).

On a contrasting note, when focusing on E_{HOMO}, **20** demonstrates the highest energy level (−5.9851 eV), followed closely by **22** with the second highest E_{HOMO} (−6.1778 eV). These values signify the pronounced potential of **20** and **22** to donate electrons (Yele *et al.*, 2021). Remarkably, capecitabine emerges as the only standard drug displaying HOMO energies higher than the synthesized compounds (**19** and **23**), boasting an energy level of E_{HOMO} = −6.4578 eV. Beyond mere energy levels, a thorough structural analysis encompasses a comprehensive evaluation of intra-ligand interactions. Notably, these interactions include hydrogen bonds (within a 3.5 Å range), halogen bonds (within a 3.5 Å range), π–π stacking (within a 5.5 Å range) and π–cation interactions (within a 6.6 Å range).

Delving deeper into the molecular architecture, both the HOMO and the LUMO orbitals exhibit localization on both arene rings of **17**. However, no discernible hydrogen bonds or π–π stacking within the studied distances are exhibited by the compound. In the intricate case of **20**, HOMO orbitals predominantly localize on the arene ring bearing the Br atom, while the LUMO orbitals are positioned closer to the imine functionality (C═N). This arrangement leads to the identification of hydrogen bonding within the optimized structure of **20**, specifically involving C═N···OH (1.50 Å) and a weaker S═O···H(aromatic) interaction (Fig. 2).

Similarly, Schiff base **21** (Fig. 3) showcases HOMO orbitals predominantly on the bromine-bearing arene ring, while the LUMO orbitals position themselves in proximity to the imine functionality. Notably, **21** boasts robust hydrogen bonding between the hydroxy O and imine N atom (1.50 Å). Extending this pattern, derivatives **18** and **19** exhibit comparable hydrogen bonding to **21**, with distances of 1.70 and 1.73 Å, respectively. Schiff base **19** (Fig. 4) distinguishes itself further by showcasing an additional, albeit weaker, hydrogen bond (2.67 Å) between the S═O group and an aromatic H atom.

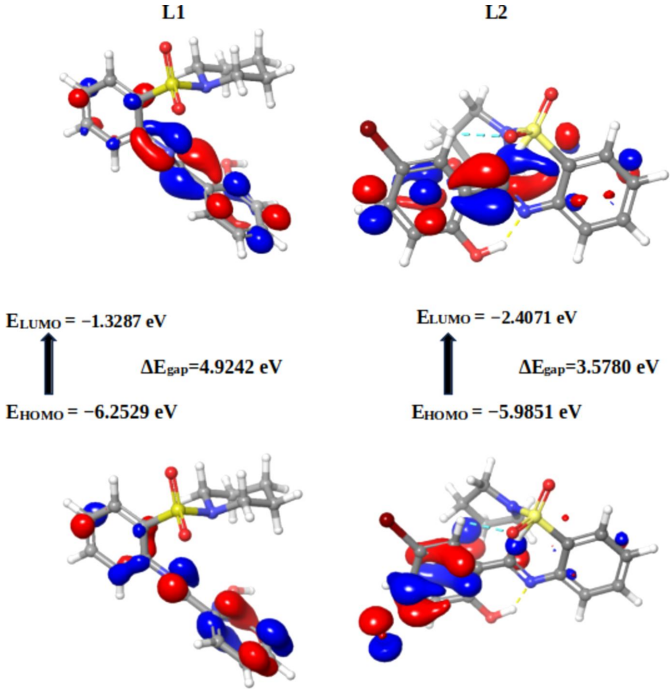

Figure 2
Frontier molecular orbitals (FMOs) of **17** and **20**.

The thematic consistency in the HOMO and LUMO orbital localization is mirrored across Schiff bases **18**, **19**, **22** and **23**, closely resembling the pattern exhibited by **20**, except for **23**, where the LUMO orbitals predominantly localize on the NO_2 group (Fig. 5).

Within the structures of 5-fluorouracil and trifluridine (Fig. 6), the HOMO and LUMO exhibit localization in distinct

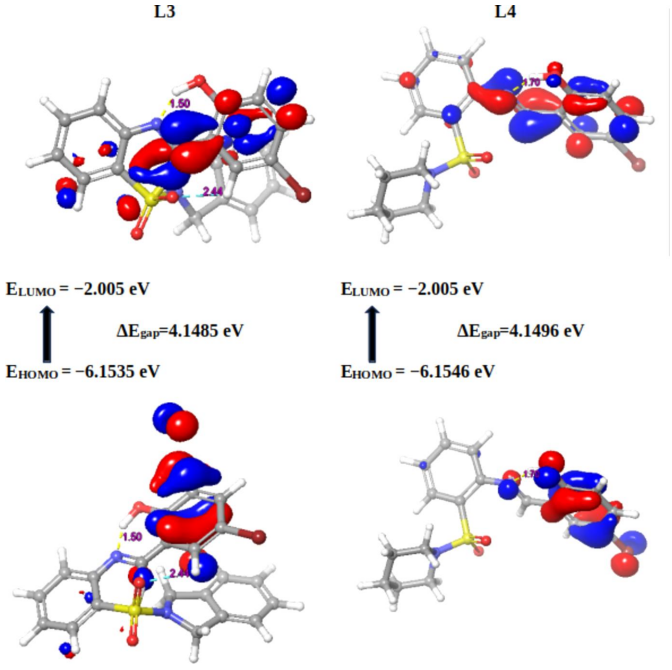

Figure 3
Frontier molecular orbitals (FMOs) of **21** and **18**.

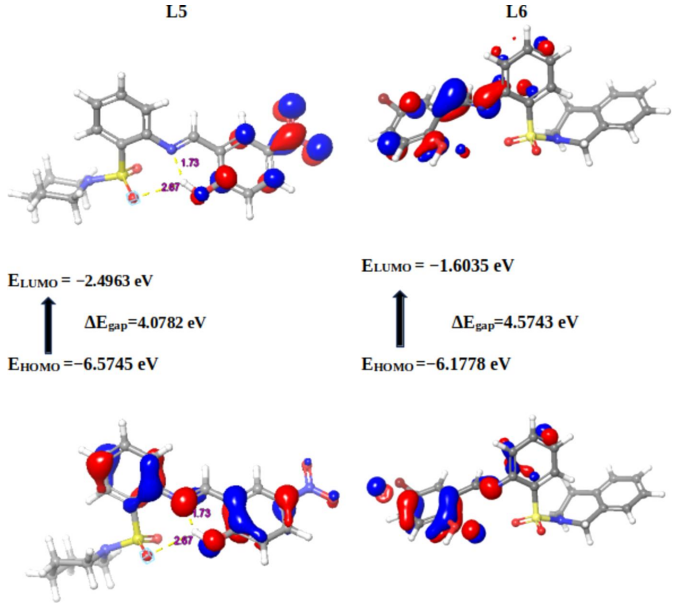

Figure 4
Frontier molecular orbitals (FMOs) of **19** and **22**.

regions of each respective molecule. This localization directly signifies the occurrence of charge-transfer processes.

Turning our focus to broader implications, the eigenvalues of the HOMO and LUMO, along with their energy gap, offer crucial insights into the biological activity of a molecule (Table 3). A diminished energy gap, symbolized as ΔE_{gap}, renders a molecule more susceptible to polarization. This phenomenon aligns with heightened chemical reactivity and reduced kinetic stability, ultimately driving positive impetus toward biological activity. In contrast, an enlarged energy gap between the HOMO and LUMO orbitals signifies the kinetic instability of a molecule, translating to a diminished propensity for biological activity (Pereira *et al.*, 2017; Akman, 2019; Choudhary *et al.*, 2013; Abdelsalam *et al.*, 2022). Adding a layer of nuance, **20** emerges as the molecule showcasing the

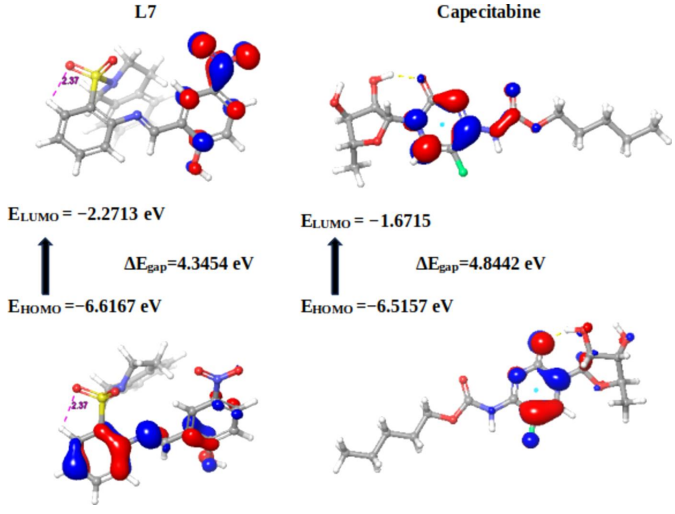

Figure 5
Frontier molecular orbitals (FMOs) of **23** and capecitabine.

Table 3
Global reactivity descriptors of the synthesized Schiff bases and standard drugs.

Entry	E_{HOMO}	E_{LUMO}	ΔE_{gap}	I	A	μ	X	η	S	ω
17	−6.2529	−1.3287	4.9242	6.2529	1.3287	−3.7908	3.7908	2.4621	0.4062	2.9183
20	−5.9851	−2.4071	3.5780	5.9851	2.4071	−4.1961	4.1961	1.7890	0.5590	4.9210
21	−6.1535	−2.0050	4.1485	6.1535	2.0050	−4.0793	4.0793	2.0743	0.4821	4.0112
18	−6.1546	−2.0050	4.1496	6.1546	2.0050	−4.0798	4.0798	2.0748	0.4820	4.0112
19	−6.5745	−2.4963	4.0782	6.5745	2.4963	−4.5354	4.5354	2.0391	0.4904	5.0439
22	−6.1778	−1.6035	4.5743	6.1778	1.6035	−3.8907	3.8907	2.2872	0.4372	3.3092
23	−6.6167	−2.2713	4.3454	6.6167	2.2713	−4.4440	4.4440	2.1727	0.4603	4.5448
5-Flu	−6.7827	−1.2659	5.5168	6.7827	1.2659	−4.0243	4.0243	2.7584	0.3625	2.9355
Cap	−6.4578	−1.6019	4.8559	6.4578	1.6019	−4.0299	4.0299	2.4279	0.4119	3.3444
Tri	−6.9868	−1.3725	5.6143	6.9868	1.3725	−4.1797	4.1797	2.8071	0.3562	3.1117

Notes: ΔE_{gap} is the energy gap or charge separation, I is ionization potential, A is electron affinity, μ is chemical potential, X is electronegativity, η is global hardness, S is global softness and ω is the electrophilicity index. Tri is trifluridine, Cap is capecitabine and 5-Flu is 5-fluorouracil.

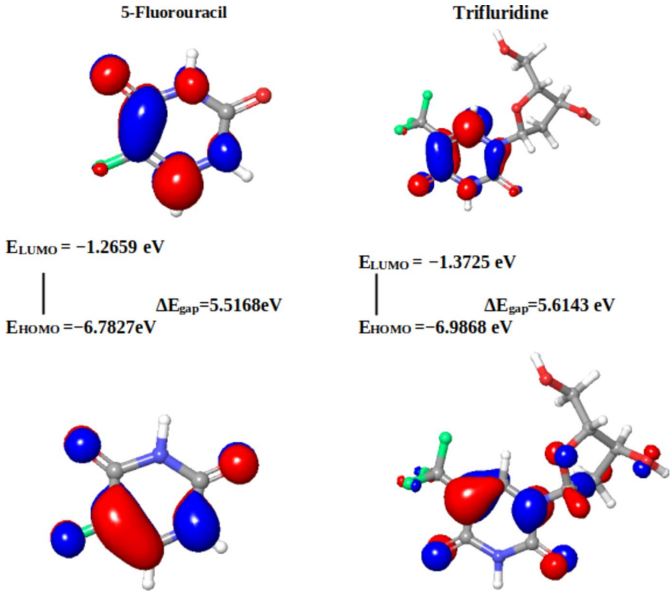

Figure 6
Frontier molecular orbitals (FMOs) of 5-fluorouracil and trifluridine.

smallest charge separation (ΔE_{gap} = 3.5780 eV), suggesting its heightened potential for biological properties. In contrast, **17** displays the largest charge separation (ΔE_{gap} = 4.9242 eV), indicating a comparatively lower propensity for biological properties compared to the other synthesized Schiff bases.

In essence, the meticulous unravelling of these quantum features through DFT provides a profound understanding of the intricate interplay between molecular structure, reactivity and biological performance. Such insights hold transformative potential in advancing drug design and precision chemical manipulation. The distinctiveness of ligand **20** is further underscored by its characterization as the 'softest' molecule (S = 0.5589 eV) and, consequently, the 'least hard' molecule (η = 1.7890 eV). Conversely, **17** exhibits the highest hardness value (η = 2.4621 eV) and lowest softness (S = 0.4062 eV). When we turn our attention to standard drugs, the order of softness is observed as capecitabine > 5-fluorouracil > trifluridine, with all values generally lower than most synthesized Schiff bases. The chemical potential (μ) spans from −4.5354 eV (lowest) for **19** to −3.7908 eV (highest) for **17**. Schiff bases **19** and **20** exhibit the highest electrophilicity index (ω), with values of 5.044 and 4.9209 eV, respectively. In contrast, Schiff base **17** showcases the lowest electrophilicity index (ω = 2.9182 eV).

With regard to the computed global reactivity indices and the HOMO–LUMO gap, the order is: **20** > **19** > **21** > **18** > **23** > **22** > capecitabine > **17** > 5-fluorouracil > trifluridine. This insightful hierarchy provides valuable direction for the reac-

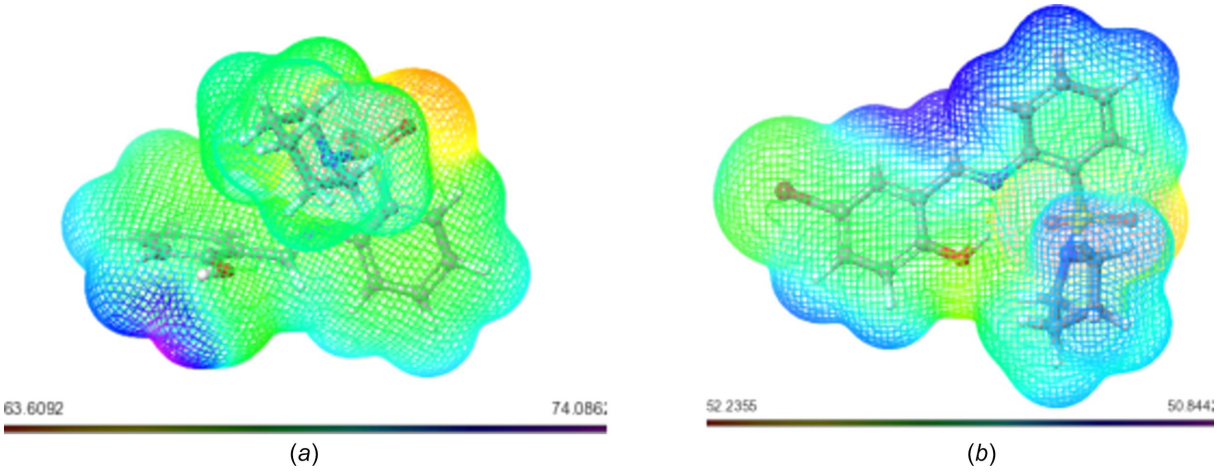

(*a*) (*b*)

Figure 7
MESP plots of (*a*) **17** and (*b*) **20**. Regions of attractive potential appear in red and those of repulsive potential appear in blue.

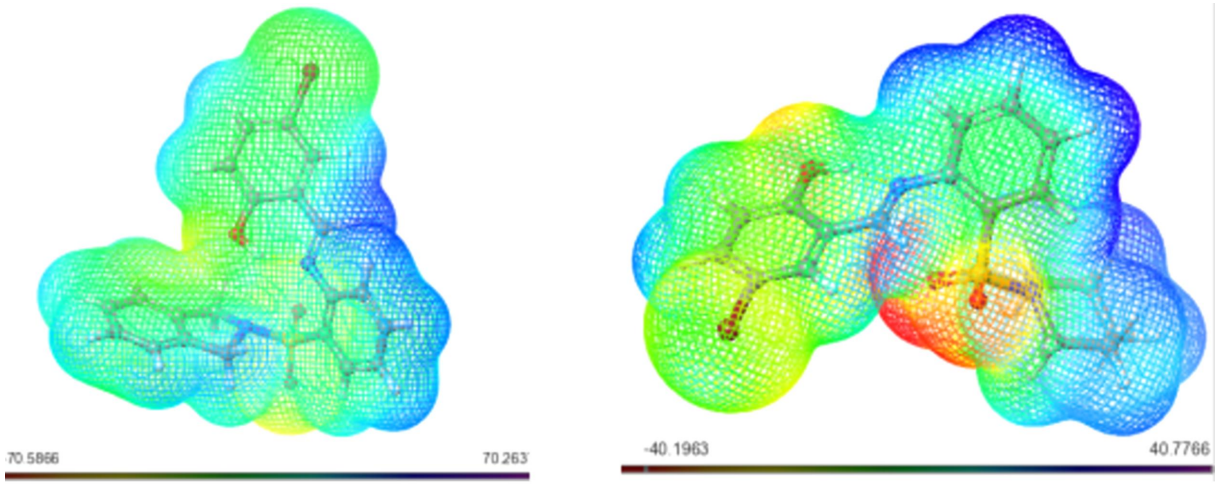

(*a*) (*b*)

Figure 8
MESP plots of (*a*) **21** and (*b*) **18**.

tivity and potential biological activity of the synthesized Schiff bases.

3.3.3. Molecular Electrostatic Potential (MESP). The Molecular Electrostatic Potential (MESP) concept serves as a window into the intricate charge distribution enveloping molecules within the expanse of three-dimensional space. Its significance is particularly pronounced in identifying susceptible loci for electrophilic and nucleophilic interactions, which are critical in the realm of biological recognition and hydrogen-bonding phenomena. Through the utilization of colour mapping grounded in electron density, the electrostatic potential of the studied molecules found visual expression, as illustrated in Figs. 2–6.

This visual representation employs a spectrum of colours to delineate the MESP surface characteristics. Red hues signify regions enriched with electrons, indicating a partially negative charge, while blue shades indicate electron-deficient zones with a partial positive charge. Light-blue nuances mark slightly electron-deficient areas, while yellow tinges highlight slightly electron-rich regions. Neutral zones with a zero potential are depicted in green (Altürk *et al.*, 2015; Friesner *et al.*, 2006).

Upon scrutinizing the MESP mappings of individual compounds, distinct patterns emerge. Schiff base **17** [Fig. 7(*a*)] predominantly reveals a green surface, save for the hydroxy-functionalized section which distinctly appears in blue. Similarly, the MESP profile of compound **20** [Fig. 7(*b*)] features prevalent blue regions, with a specific green–yellow region localized over the bromine-bearing arene ring. In the case of **21** [Fig. 8(*a*)], an evident gradient from green to blue characterizes the MESP map. Analogously, the MESP portrayal of **18** [Fig. 9(*b*)] reflects this trend, except for the S═O functional-group regions which assume a red hue. Both **19** [Fig. 9(*a*)] and **22** [Fig. 9(*b*)] display a blending of blue and green regions in their respective MESP renderings. For **23** [Fig. 10(*a*)], the MESP map predominantly features green hues, while the hydroxy-enriched area adopts a distinctive blue shade. Noteworthy instances include the standard drug capecitabine [Fig. 10(*b*)], predominantly depicted in blue in its MESP representation. The standard drug 5-fluorouracil

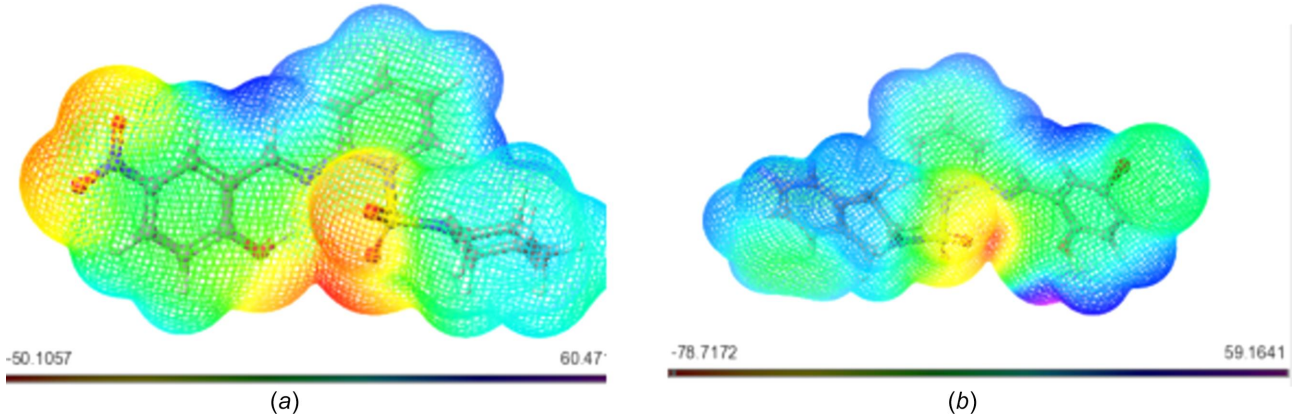

(*a*) (*b*)

Figure 9
MESP plots of (*a*) **19** and (*b*) **22**.

Table 4
Summary of the binding energy (kcal mol^{-1}) of Schiff bases with poly(ADP-ribose) polymerase.

Optimized Schiff bases	Summarized drug-likeness and toxicity	6kro
6kro_23_E=714.59	mildly nondrug-like and toxic	−11.1
6kro_22_E=797.81	nontoxic but mildly nondrug-like	−10.3
6kro_21_E=687.32	nondrug-like and nontoxic	−9.9
6kro_20_E=635.91	drug-like and nontoxic	−9.5
6kro_17_E=666.05	drug-like and nontoxic	−9.2
6kro_18_E=685.47	drug-like and nontoxic	−8.7
6kro_19_E=748.77	drug-like but mildly toxic	−6.7
6kro_trifluridine_E=282.80	drug-like but mildly toxic	−8
6kro_capecitabine_E=624.15	drug-like but highly toxic	−7.9
6kro_5-fluorouracil_E=45.84	mildly nondrug-like and toxic	−5.5

Table 5
In-silico toxicity study and drug-likeness of **20** using ProTox-II and SwissADME.

Druglikeness

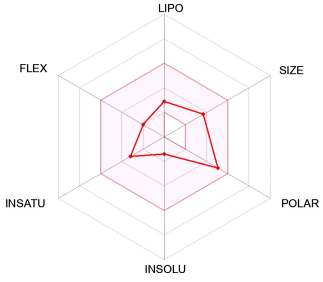

Toxicity

Target	Prediction	Probability
Hepatotoxicity	Inactive	0.57
Carcinogenicity	Inactive	0.57
Immunotoxicity	Inactive	0.87
Mutagenicity	Inactive	0.71
Cytotoxicity	Inactive	0.73

[Fig. 11(*a*)] showcases the entire spectrum of colour variations across its surface. Similarly, trifluridine [Fig. 11(*b*)] transitions from blue to red, thereby illustrating its surface

Table 6
In-silico toxicity study and drug-likeness of **23** using ProTox-II and SwissADME.

Druglikeness

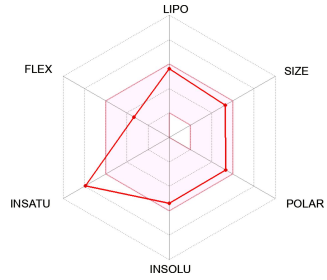

Toxicity

Target	Prediction	Probability
Hepatotoxicity	Inactive	0.62
Carcinogenicity	Inactive	0.57
Immunotoxicity	Inactive	0.94
Mutagenicity	Active	0.68
Cytotoxicity	Inactive	0.78

characteristics encompassing the 2-(hydroxymethyl)tetrahydrofuran-3-ol moiety.

3.4. Docking studies

3.4.1. Schiff bases as potential inhibitors of tankyrase colon cancer protein molecules. The docking carried out using *AutoDock Vina* on the PyRx website (https://pyrx.sourceforge.io/) and the summary of the binding energy of each ligand obtained is presented in Table 4 (the structures are presented in Fig. 12). In addition, the drug-likeness and toxicity of the synthesized Schiff bases and reference drugs were also investigated (Tables 5–10).

It is noteworthy that ligand **23** has the highest binding energy of −11.1 kcal mol^{-1}, probably due to the presence of not only the sulfonamide but also the nitro group coupled with the tetrahydroisoquinoline moiety binding to the protein.

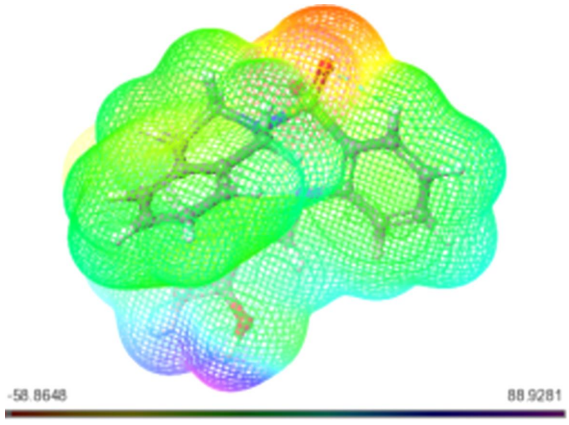

(*a*)

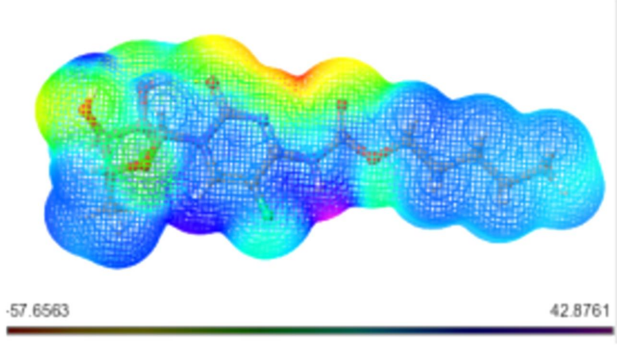

(*b*)

Figure 10
MESP plots of (*a*) **23** and (*b*) capecitabine.

Table 7
In-silico toxicity study and drug-likeness of trifluridine.

Druglikeness	
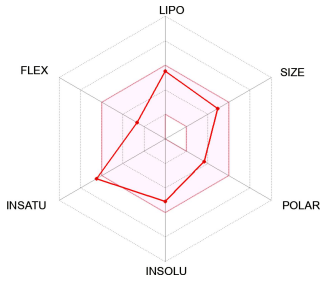	

Toxicity		
Target	Prediction	Probability
Hepatotoxicity	Inactive	0.76
Carcinogenicity	Inactive	0.60
Immunotoxicity	Inactive	0.99
Mutagenicity	Active	0.64
Cytotoxicity	Inactive	0.88

Table 8
In-silico toxicity study and drug-likeness of 5-fluorouracil.

Druglikeness	
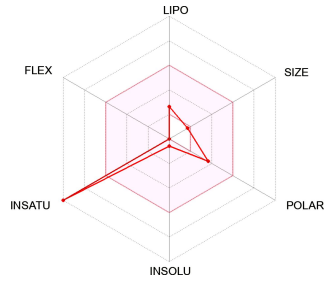	

Toxicity		
Target	Prediction	Probability
Hepatotoxicity	Inactive	0.78
Carcinogenicity	Active	0.85
Immunotoxicity	Inactive	0.99
Mutagenicity	Inactive	0.88
Cytotoxicity	Inactive	0.93

The binding energy was observed to be significantly higher than that of the reference drugs trifluridine, capecitabine and 5-fluorouracil having binding energies of −8.0, −7.9 and −5.5 kcal mol^{-1}, respectively. However, when the toxicity and the drug-likeness of ligand **23** were checked using the ProTox-II webserver and SwissADME (http://www.swissadme.ch/), respectively, it was toxic and failed some of the rules despite its excellent binding interaction.

Interestingly, ligands **17**, **20** and **18** were completely non-toxic and followed all drug-likeness rules, unlike all the other synthesized Schiff bases (*i.e.* **21**, **19**, **22** and **23**; see supporting information). In comparison, the reference drugs were also toxic, falling short of at least one drug-likeness rule. The best reference drug, *i.e.* trifluridine, and ligand **20**, namely, (*E*)-4-bromo-2-({[2-(pyrrolidin-1-ylsulfonyl)phenyl]imino}methyl) phenol, with the best binding energy and in compliance with all drug-like rules and displaying complete nontoxicity, were selected for further study (Table 10).

The 2D and 3D structures of **20** showing the interacting amino acid residues [Fig. 13(*a*)], bond lengths [Fig. 13(*b*)], hydrophobic interactions [Fig. 13(*c*)] and solvent-accessibility surface [Fig. 13(*d*)] are all presented. One of the sulfonamide O atoms exhibits a hydrogen-bonding interaction with amino acid residue Arg_{1100} at a bonding distance of 1.97 Å, which is also noticeable within the atoms of the ligand in an intramolecular fashion [Figs. 13(*a*) and 13(*b*)]. π-Alkyl and T-shaped interactions were also exhibited between the pyrrolidine moiety and amino acid residues Val_{1000} and Leu_{1097}, and between the π-electrons of the two aromatic rings and the Trp_{1006} and Tyr_{1009} residues, respectively.

Significantly, the amino acid residues interacting with tankyrase poly(ADP-ribose) polymerase residues prefer

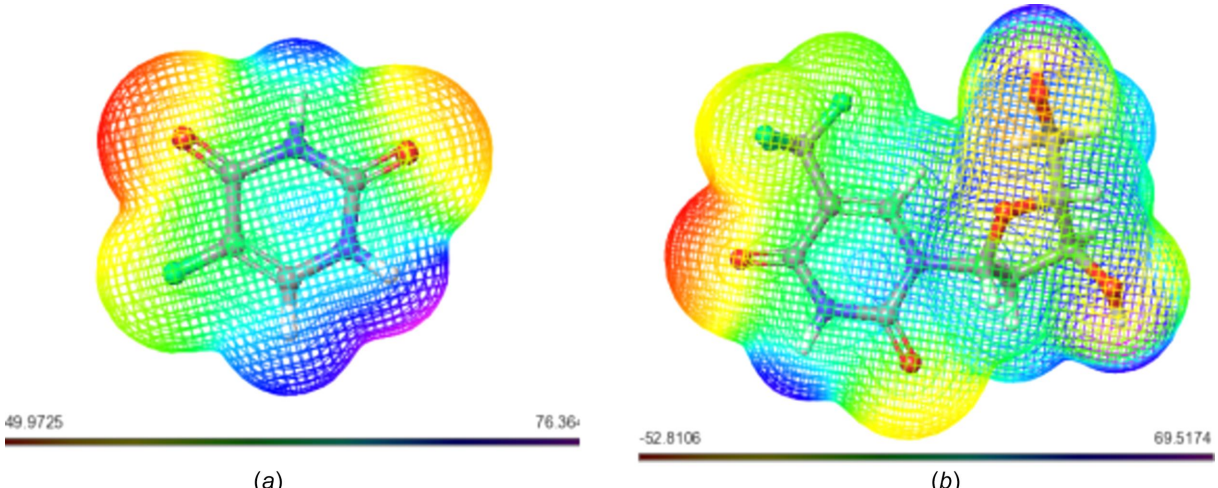

Figure 11
MESP plots of (*a*) 5-fluorouracil and (*b*) trifluridine.

Table 9
Physicochemical properties of the synthesized Schiff bases and reference drugs.

Compound	M_r	No. of heavy atoms	Fraction Csp^3	No. rotational bonds	No. hydrogen-bond acceptors	No. hydrogen-bond donors	TPSA	log *Kp* (cm s^{-1})	Bioavailability score
17	344.43	24	0.28	4	5	1	78.35	−6.37	0.55
20	409.3	24	0.24	4	5	1	78.35	−6.53	0.55
21	457.34	28	0.10	4	4	1	78.35	−6.04	0.55
18	423.32	25	0.28	4	5	1	78.35	−6.36	0.55
19	389.43	27	0.28	5	7	1	124.17	−6.77	0.55
22	471.37	29	0.14	4	5	1	78.35	−6.17	0.55
23	437.47	31	0.14	5	7	1	124.17	−6.58	0.55
Trifluridine	296.2	20	0.60	3	8	3	104.55	−8.43	0.55
Capecitabine	359.35	25	0.67	8	8	3	122.91	−8.09	0.55
5-Fluorouracil	130.08	9	0	0	3	2	65.72	−7.73	0.55

hydrophobic interactions [as depicted by the deep-brown region of Fig. 13(*c*)]. While Arg_{1100} had good solvent-accessibility surface interactions, other interacting residues had excellent solvent interactions with ligand **20** [Figs. 13(*c*) and 13(*d*)]. Although the reference drug trifluridine has two hydrogen-bond interactions, they are comparatively weaker and have longer bond lengths of 2.14 and 2.60 Å with Gly1032 and Asp1045, respectively, when compared with ligand **20** (1.90 Å), as presented in Figs. 14(*a*) and 14(*b*).

Noticeably, the solvent-accessibility surface of the reference drug seems better, as all interacting amino acid residues interact in the blue region [Fig. 14(*d*)]; however, it has comparably lower binding energy (Table 4), *i.e.* poorer hydrophobicity than exhibited by most drug-like candidates [Fig. 14(*c*)], and it possesses mutagenic toxicity (Table 7).

3.4.2. Toxicity and drug-likeness of Schiff bases 17–23 and reference drugs. The SMILES (simplified molecular-input line-entry system) of the synthesized Schiff bases and the reference drugs were obtained *via ChemDraw* (Version 14.0) software and *PubChem*, respectively. These SMILES were uploaded into the online webservers Pro-Tox-II and SwissADME to investigate the *in-silico* toxicity and drug-likeness. A summary of the results obtained is presented in Tables 5–10. From the results, it is obvious that ligand **23** (−11.10 kJ mol^{-1}) fell short of the toxicity test, despite being the best interacting ligand (Table 7). It could also not completely fit into the hexagonal drug-likeness physicochemical space. From the investigation, it became clear that ligand **20**, with a binding energy of −9.50 kJ mol^{-1}, is completely nontoxic and fits perfectly into the hexagon, thereby displaying 100% drug-likeness (Table 6).

In comparison, the two common colon cancer reference drugs used in this study show some levels of toxicity. While trifluridine is mildly mutagenic, 5-fluorouracil is highly carcinogenic (Tables 8 and 9). Unlike synthesized Schiff bases **17**, **20** and **18**, this study also reveals that 5-fluorouracil fails some drug-likeness tests in addition to its toxic nature (Table 9).

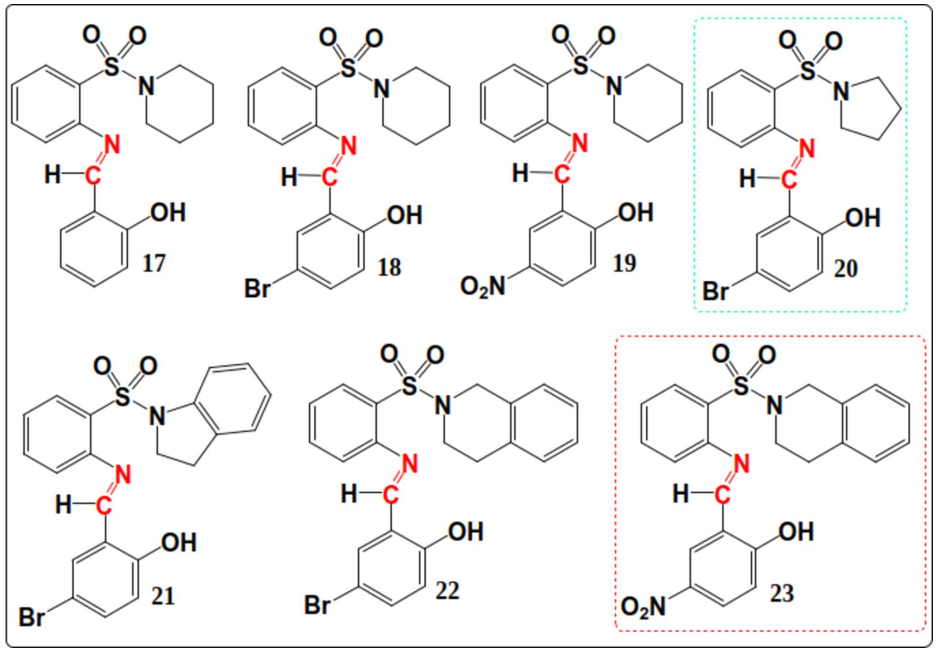

Figure 12
Structures of the synthesized Schiff bases **17**–**23** used for docking.

Table 10
Drug-likeness rule violation and *in-silico* toxicity study of trifluridine and 5-fluorouracil for comparison.

GI is gastrointestinal and BBB is blood–brain barrier.

	Drug-likeness rules violations					Blood–brain distribution and metabolism	
Compounds	Lipinski	Ghose	Veber	Egan	Muegge	GI absorption	BBB permeant
17	0	0	0	0	0	High	No
20	0	0	0	0	0	High	No
21	0	0	0	0	0	High	No
18	0	0	0	0	0	High	No
19	0	0	0	0	0	High	No
22	0	0	0	0	0	Low	No
23	0	0	0	0	0	High	No
Trifluridine	0	0	0	0	0	High	No
Capecitabine	0	0	0	0	0	High	No
5-Fluorouracil	0	0	0	0	0	High	No

In the course of the drug-likeness investigation, physicochemical parameters and drug-likeness violations of the Schiff bases and the reference drugs trifluridine and 5-fluorouracil were also compared, as shown in Tables 9 and 10. Most of the properties, such as the number of heavy atoms, rotatable bonds, TPSA (topological polar surface area), log *Kp* and bioavailability scores of the synthesized ligands compare effectively with trifluridine and 5-fluorouracil. Interestingly, none of the synthesized ligands violated Absorption, Distribution, Metabolism and Excretion (ADME) rules; hence, they can be tagged as potential drug candidates. While their gastrointestinal (GI) absorption is very high, the same prop-

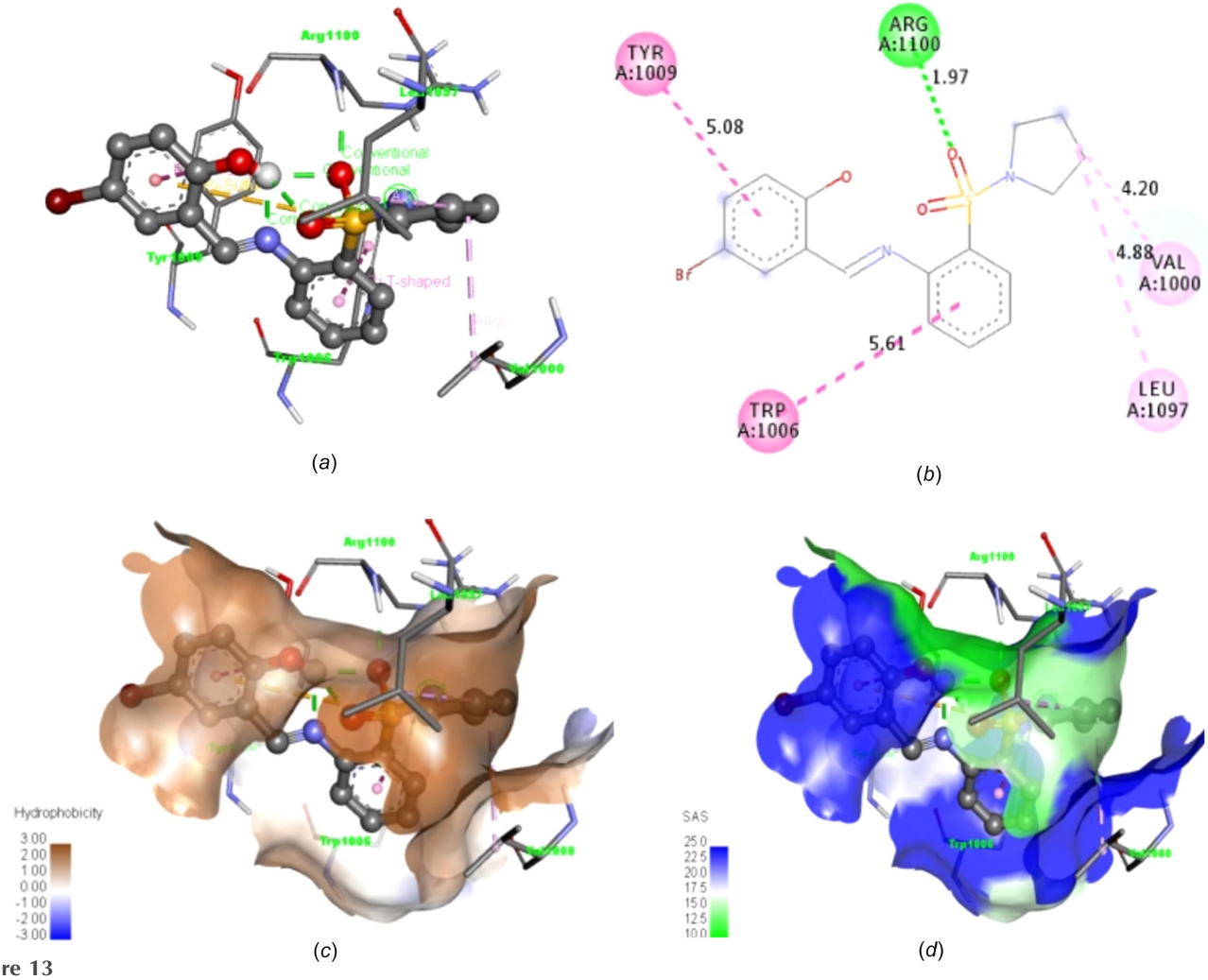

Figure 13
2D and 3D structures of synthesized Schiff base **20** showing (*a*) the interacting amino acid residues, (*b*) bond lengths, (*c*) hydrophobic interactions and (*d*) solvent-accessibility surface.

erties exhibited by the reference drugs, none of the Schiff bases are blood–brain barrier permeant, making them safe without any unwarranted interference with the central nervous system (Table 9).

4. Conclusion

The successful synthesis, characterization and analysis of the intermolecular interactions of N^1-(5^1-substituted-2^1-hydroxybenzylidenyl)-*N*-cycloamino-2-sulfanilamides (compounds **17**–**23**) have been achieved, alongside their evaluation for inhibitory effects on tankyrase poly(ADP-ribose) polymerase in the context of colon cancer through *in-silico* testing. Crystal packing and density functional theory (DFT) analyses have indicated that hydrogen bonds and π–π stacking play a crucial role in the molecular cohesion of these compounds. Furthermore, the DFT results, when combined with molecular docking studies, reveal that the electronegativity and electrophilicity attributes of these compounds significantly influence their binding affinity towards tankyrase poly(ADP-ribose) polymerase. This comprehensive study not only sheds light on the underlying mechanisms of action but also lays down a foundational framework for the development of effective therapies against colon cancer based on compounds **17**–**23**.

Acknowledgements

This project was graciously funded by the University of Lagos Central Research Committee, the Nigerian Government's TetFund IBR and the National Research Foundation (NRF) of South Africa. We extend our gratitude to the Center for High Performance Computing (CHPC) in Cape Town, South Africa, for furnishing the necessary computational resources on the Schrödinger Platform that facilitated our molecular modelling studies focused on protein preparation. It is important to note that the authors declare no financial or non-financial conflicts of interest related to this study. The conceptual framework and design of the research were collaboratively developed by all contributing authors. Material preparation, data collection and analysis were performed by Sherif O. Kolade, Eric C. Hosten, Allen T. Gordon, Idris A. Olasupo and Olayinka T. Asekun. The first draft of the

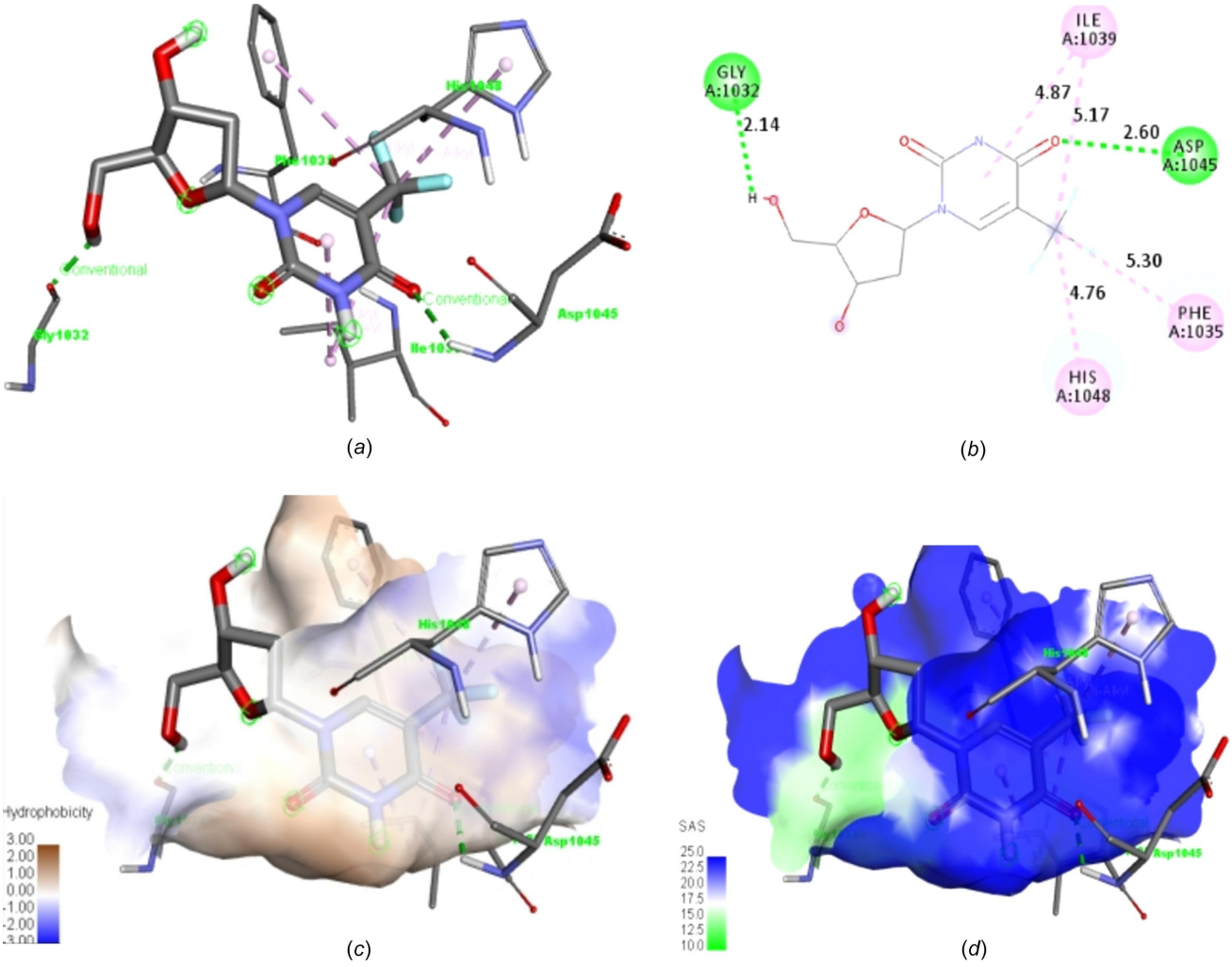

Figure 14
2D and 3D structures of the reference drug trifluridine, showing (*a*) the interacting amino acid residues, (*b*) bond lengths, (*c*) hydrophobic interactions and (*d*) solvent-accessibility surface.

manuscript was written by Sherif O. Kolade, Adeniyi S. Ogunlaja and Oluwole B. Familoni, and all authors commented on previous versions of the manuscript. All authors read and approved the final manuscript.

Funding information

The following funding is acknowledged: University of Lagos Central Research Committee (grant No. CRC 2015/25 to Oluwole Familoni); Nigerian Government TETFund IBR (grant No. CRC/TETFUND 2018/016 to Oluwole Familoni); National Research Foundation (NRF) of South Africa (grant No. 129887 to Adeniyi Ogunlaja).

References

Abdelsalam, M. M., Bedair, M. A., Hassan, A. M., Heakal, B. H., Younis, A., Elbialy, Z. I., Badawy, M. A., Fawzy, H. E. & Fareed, S. A. (2022). *Arabian J. Chem.* **15**, 103491.

Abd El-Wahab, H., Abd El-Fattah, M., El-alfy, H. M. Z., Owda, M. E., Lin, L. & Hamdy, I. (2020). *Prog. Org. Coat.* **142**, 105577.

Abd-Elzaher, M. M., Labib, A. A., Mousa, H. A., Moustafa, S. A., Ali, M. M. & El-Rashedy, A. A. (2016). *Beni-Suef Univ. J. Basic Appl. Sci.* **5**, 85–96.

Afsan, Z., Roisnel, T., Tabassum, S. & Arjmand, F. (2020). *Bioorg. Chem.* **94**, 103427.

Akman, F. (2019). *Cellul. Chem. Technol.* **53**, 243–250.

Alblewi, F. F., Alsehli, M. H., Hritani, Z. M., Eskandrani, A., Alsaedi, W. H., Alawad, M. O., Elhenawy, A. A., Ahmed, H. Y., El-Gaby, M. S. A., Afifi, T. H. & Okasha, R. M. (2023). *Int. J. Mol. Sci.* **24**, 16716.

Altürk, S., Tamer, Ö., Avcı, D. & Atalay, Y. (2015). *J. Organomet. Chem.* **797**, 110–119.

Becke, A. D. (1993). *J. Chem. Phys.* **98**, 5648–5652.

Behrens, J. (2000). *Ann. N. Y. Acad. Sci.* **910**, 21–35.

Bruker (2016). *APEX2*, *SAINT*, *SADABS* and *TWINABS*. Bruker AXS Inc., Madison, Wisconsin, USA.

Choudhary, N., Bee, S., Gupta, A. & Tandon, P. (2013). *Comput. Theor. Chem.* **1016**, 8–21.

Dassault Systémes (2020). *Discovery Studio*. BIOVIA, San Diego, CA, USA. https://www.3ds.com/.

Dueke-Eze, C. U., Fasina, T. M., Oluwalana, A. E., Familoni, O. B., Mphalele, J. M. & Onubuogu, C. (2020). *Sci. Afr.* **9**, e00522.

Eisemann, T. & Pascal, J. M. (2020). *Cell. Mol. Life Sci.* **77**, 19–33.

Elsamra, R. M., Masoud, M. S. & Ramadan, A. M. (2022). *Sci. Rep.* **12**, 20192.

Farrugia, L. J. (2012). *J. Appl. Cryst.* **45**, 849–854.

Feng, X. & Koh, D. W. (2013). *Int. Rev. Cell Mol. Biol.* **304**, 227–281.

Friesner, R. A., Murphy, R. B., Repasky, M. P., Frye, L. L., Greenwood, J. R., Halgren, T. A., Sanschagrin, P. C. & Mainz, D. T. (2006). *J. Med. Chem.* **49**, 6177–6196.

Gao, C., Xiao, G. & Hu, J. (2014). *Cell Biosci.* **4**, 13.

Gordon, A. T., Hosten, E. C. & Ogunlaja, A. S. (2022). *Pharmaceuticals*, **15**, 1240.

Hall, M. L., Goldfeld, D. A., Bochevarov, A. D. & Friesner, R. A. (2009). *J. Chem. Theory Comput.* **5**, 2996–3009.

Huang, H. & He, X. (2008). *Curr. Opin. Cell Biol.* **20**, 119–125.

Hübschle, C. B., Sheldrick, G. M. & Dittrich, B. (2011). *J. Appl. Cryst.* **44**, 1281–1284.

Irfan, A., Rubab, L., Rehman, M. U., Anjum, R., Ullah, S., Marjana, M., Qadeer, S. & Sana, S. (2020). *Heterocycl. Commun.* **26**, 46–59.

Jędrzejczyk, M., Janczak, J. & Huczyński, A. (2022). *J. Mol. Struct.* **1263**, 133129.

Kolade, S. O., Izunobi, J. U., Gordon, A. T., Hosten, E. C., Olasupo, I. A., Ogunlaja, A. S., Asekun, O. T. & Familoni, O. B. (2022). *Acta Cryst.* C**78**, 730–742.

Kolade, S. O., Izunobi, J. U., Hosten, E. C., Olasupo, I. A., Ogunlaja, A. S. & Familoni, O. B. (2020). *Acta Cryst.* C**76**, 810–820.

Kondapuram, S. K., Sarvagalla, S. & Coumar, M. S. (2021). In *Molecular Docking for Comput-Aided Drug Design*, pp. 463–477. New York: Academic Press.

Kumar, A., Bhagat, K. K., Singh, A. K., Singh, H., Angre, T., Verma, A., Khalilullah, H., Jaremko, M., Emwas, A. H. & Kumar, P. (2023*a*). *RSC Adv.* **13**, 6872–6908.

Kumar, A., Singh, A. K., Singh, H., Vijayan, V., Kumar, D., Naik, J. & Kumar, P. (2023*b*). *Pharmaceuticals*, **16**, 299.

Macrae, C. F., Sovago, I., Cottrell, S. J., Galek, P. T. A., McCabe, P., Pidcock, E., Platings, M., Shields, G. P., Stevens, J. S., Towler, M. & Wood, P. A. (2020). *J. Appl. Cryst.* **53**, 226–235.

Mahmood, A., Irfan, A. & Wang, J. L. (2022). *Chem. Eur. J.* **28**, e202103712.

Matela, G. (2020). *Anticancer Agents Med. Chem.* **20**, 1908–1917.

Meyer, R. G., Meyer-Ficca, M. L., Jacobson, E. L. & Jacobson, M. K. (2006). *Enzymes in poly(ADP-ribose) metabolism*, edited by A. Bürkle, pp. 1–12. Georgetown: Landes Bioscience.

Muhammad-Ali, M. A., Jasim, E. Q. & Al-Saadoon, A. H. (2023). *J. Med. Chem. Sci.* **6**, 2128–2139.

Pai, S. G., Carneiro, B. A., Mota, J. M., Costa, R., Leite, C. A., Barroso-Sousa, R. & Giles, F. J. (2017). *J. Hematol. Oncol.* **10**, 101.

Pandi, S., Kulanthaivel, L., Subbaraj, G. K., Rajaram, S. & Subramanian, S. (2022). *BioMed Res. Int.* **2022**, 3338549.

Pawar, S. S. & Rohane, S. H. (2021). *Asian J. Res. Chem.* **14**, 86-–88.

Pereira, F., Xiao, K., Latino, D. A., Wu, C., Zhang, Q. & Aires-de-Sousa, J. (2017). *J. Chem. Inf. Model.* **57**, 11–21.

Prokopenko, Y. S., Perekhoda, L. O. & Georgiyants, V. A. (2019). *J. Appl. Pharm. Sci.* **9**, 066–072.

Salehi, M., Kubicki, M., Galini, M., Jafari, M. & Malekshah, R. E. (2019). *J. Mol. Struct.* **1180**, 595–602.

Sheldrick, G. M. (2015*a*). *Acta Cryst.* A**71**, 3–8.

Sheldrick, G. M. (2015*b*). *Acta Cryst.* C**71**, 3–8.

Shirai, F., Mizutani, A., Yashiroda, Y., Tsumura, T., Kano, Y., Muramatsu, Y., Chikada, T., Yuki, H., Niwa, H., Sato, S., Washizuka, K., Koda, Y., Mazaki, Y., Jang, M. K., Yoshida, H., Nagamori, A., Okue, M., Watanabe, T., Kitamura, K., Shitara, E., Honma, T., Umehara, T., Shirouzu, M., Fukami, T., Seimiya, H., Yoshida, M. & Koyama, H. (2020). *J. Med. Chem.* **63**, 4183–4204.

Silva, R. R. da, Ramalho, T. C., Santos, J. M. & Figueroa-Villar, J. D. (2006). *J. Phys. Chem. A*, **110**, 1031–1040.

Spackman, P. R., Turner, M. J., McKinnon, J. J., Wolff, S. K., Grimwood, D. J., Jayatilaka, D. & Spackman, M. A. (2021). *J. Appl. Cryst.* **54**, 1006–1011.

Spek, A. L. (2020). *Acta Cryst.* E**76**, 1–11.

Trott, O. & Olson, A. J. (2010). *J. Comput. Chem.* **31**, 455–461.

Yele, V., Sigalapalli, D. K., Jupudi, S. & Mohammed, A. A. (2021). *J. Mol. Model.* **27**, 359.

supporting information

Acta Cryst. (2024). C**80**, 129-142 [https://doi.org/10.1107/S205322962400233X]

Synthesis, crystal structure and *in-silico* evaluation of arylsulfonamide Schiff bases for potential activity against colon cancer

Sherif O. Kolade, Oluwafemi S. Aina, Allen T. Gordon, Eric C. Hosten, Idris A. Olasupo, Adeniyi S. Ogunlaja, Olayinka T. Asekun and Oluwole B. Familoni

Computing details

4-Bromo-2-{*N*-[2-(piperidine-1-sulfonyl)phenyl]carboximidoyl}phenol

Crystal data

$C_{18}H_{19}BrN_2O_3S$
M_r = 423.32
Orthorhombic, *Pbca*
a = 12.4070 (9) Å
b = 17.4250 (14) Å
c = 17.5276 (12) Å
V = 3789.3 (5) Å^3
Z = 8
F(000) = 1728
D_x = 1.484 Mg m^{-3}
Melting point: 427.45 K
Mo *Kα* radiation, λ = 0.71073 Å
Cell parameters from 9105 reflections
θ = 2.3–24.5°
μ = 2.30 mm^{-1}
T = 296 K
Platelet, yellow
0.84 × 0.43 × 0.12 mm

Data collection

Bruker APEXII CCD diffractometer
Radiation source: sealed tube
Graphite monochromator
Detector resolution: 8.3333 pixels mm^{-1}
φ and ω scans
Absorption correction: multi-scan (SADABS; Bruker, 2016)
T_{min} = 0.133, T_{max} = 0.241
27860 measured reflections
3356 independent reflections
2255 reflections with $I > 2\sigma(I)$
R_{int} = 0.060
θ_{max} = 25.1°, θ_{min} = 2.3°
h = −14→14
k = −19→20
l = −20→20

Refinement

Refinement on F^2
Least-squares matrix: full
$R[F^2 > 2\sigma(F^2)]$ = 0.062
$wR(F^2)$ = 0.172
S = 1.09
3356 reflections
227 parameters
0 restraints
Primary atom site location: dual
Secondary atom site location: difference Fourier map
Hydrogen site location: inferred from neighbouring sites
H-atom parameters constrained
$w = 1/[\sigma^2(F_o^2) + (0.061P)^2 + 7.1303P]$ where $P = (F_o^2 + 2F_c^2)/3$
$(\Delta/\sigma)_{max} < 0.001$
$\Delta\rho_{max}$ = 0.52 e Å^{-3}
$\Delta\rho_{min}$ = −0.37 e Å^{-3}

Special details

Geometry. All esds (except the esd in the dihedral angle between two l.s. planes) are estimated using the full covariance matrix. The cell esds are taken into account individually in the estimation of esds in distances, angles and torsion angles; correlations between esds in cell parameters are only used when they are defined by crystal symmetry. An approximate (isotropic) treatment of cell esds is used for estimating esds involving l.s. planes.

Refinement. Carbon-bound H atoms were placed in calculated positions and were included in the refinement in the riding model approximation, with U_{iso}(H) set to 1.2 U_{eq}(C).
The H atom of the hydroxyl group was allowed to rotate with a fixed angle around the C—O bond to best fit the experimental electron density (HFIX 147 in the SHELXL program (Sheldrick, 2015)), with U_{iso}(H) set to 1.5U_{eq}(O).

Fractional atomic coordinates and isotropic or equivalent isotropic displacement parameters (Å²)

	x	*y*	*z*	U_{iso}*/U_{eq}
Br1	0.85040 (8)	0.46864 (5)	0.55005 (4)	0.1140 (4)
S1	0.56327 (10)	0.22940 (8)	0.14642 (7)	0.0607 (4)
O1	0.5496 (3)	0.4349 (3)	0.2834 (3)	0.0907 (13)
H1A	0.579549	0.413541	0.247549	0.136*
O2	0.4882 (3)	0.2902 (2)	0.1591 (2)	0.0777 (11)
O3	0.5316 (3)	0.1682 (2)	0.0968 (2)	0.0883 (12)
N1	0.6996 (3)	0.3585 (2)	0.2148 (2)	0.0555 (10)
N2	0.5983 (3)	0.1974 (2)	0.2293 (2)	0.0565 (10)
C1	0.7606 (4)	0.3689 (3)	0.2721 (3)	0.0533 (11)
H1	0.830912	0.350473	0.270688	0.064*
C11	0.7232 (4)	0.4088 (3)	0.3396 (3)	0.0543 (12)
C12	0.6188 (5)	0.4412 (3)	0.3421 (3)	0.0688 (15)
C13	0.5885 (5)	0.4815 (3)	0.4058 (4)	0.091 (2)
H13	0.520618	0.504049	0.407731	0.109*
C14	0.6568 (6)	0.4888 (4)	0.4667 (4)	0.092 (2)
H14	0.634378	0.515785	0.509646	0.111*
C15	0.7582 (5)	0.4568 (3)	0.4652 (3)	0.0752 (16)
C16	0.7913 (4)	0.4171 (3)	0.4014 (3)	0.0629 (13)
H16	0.859904	0.395629	0.400021	0.075*
C21	0.7416 (4)	0.3243 (3)	0.1480 (2)	0.0518 (11)
C22	0.6852 (4)	0.2672 (3)	0.1103 (2)	0.0521 (11)
C23	0.7250 (4)	0.2370 (3)	0.0428 (3)	0.0665 (14)
H23	0.687000	0.198557	0.017620	0.080*
C24	0.8208 (5)	0.2636 (3)	0.0126 (3)	0.0719 (15)
H24	0.846894	0.243698	−0.033050	0.086*
C25	0.8771 (5)	0.3193 (3)	0.0503 (3)	0.0678 (14)
H25	0.942106	0.336688	0.030261	0.081*
C26	0.8389 (4)	0.3502 (3)	0.1175 (3)	0.0589 (12)
H26	0.877962	0.388227	0.142523	0.071*
C31	0.6682 (5)	0.1288 (3)	0.2294 (3)	0.0813 (17)
H31A	0.719512	0.132034	0.187760	0.098*
H31B	0.624822	0.083122	0.222158	0.098*
C32	0.7269 (6)	0.1238 (4)	0.3034 (4)	0.106 (2)
H32A	0.775409	0.167263	0.308142	0.127*
H32B	0.769888	0.077342	0.304347	0.127*

C33	0.6496 (6)	0.1234 (4)	0.3696 (4)	0.105 (2)
H33A	0.689478	0.122977	0.417148	0.126*
H33B	0.605394	0.077539	0.367612	0.126*
C34	0.5783 (7)	0.1938 (4)	0.3663 (3)	0.108 (2)
H34A	0.525103	0.191096	0.406797	0.130*
H34B	0.621880	0.239270	0.374740	0.130*
C35	0.5233 (5)	0.2003 (4)	0.2927 (3)	0.0880 (19)
H35A	0.471669	0.158796	0.287800	0.106*
H35B	0.483889	0.248338	0.291006	0.106*

Atomic displacement parameters (Å²)

	U^{11}	U^{22}	U^{33}	U^{12}	U^{13}	U^{23}
Br1	0.1624 (8)	0.1126 (7)	0.0671 (4)	−0.0226 (5)	0.0104 (4)	−0.0245 (4)
S1	0.0541 (7)	0.0761 (9)	0.0518 (7)	0.0032 (6)	−0.0116 (5)	0.0084 (6)
O1	0.062 (2)	0.096 (3)	0.114 (4)	0.011 (2)	0.016 (2)	−0.026 (3)
O2	0.060 (2)	0.096 (3)	0.077 (2)	0.023 (2)	−0.0044 (18)	0.025 (2)
O3	0.086 (3)	0.113 (3)	0.066 (2)	−0.024 (2)	−0.022 (2)	−0.010 (2)
N1	0.060 (2)	0.050 (2)	0.056 (2)	0.0038 (19)	0.009 (2)	−0.0015 (19)
N2	0.058 (2)	0.058 (2)	0.054 (2)	0.0097 (19)	0.0010 (18)	0.0104 (18)
C1	0.058 (3)	0.045 (3)	0.056 (3)	0.009 (2)	0.016 (2)	−0.002 (2)
C11	0.067 (3)	0.038 (3)	0.057 (3)	−0.001 (2)	0.021 (2)	−0.002 (2)
C12	0.069 (3)	0.050 (3)	0.088 (4)	−0.006 (3)	0.031 (3)	−0.012 (3)
C13	0.076 (4)	0.073 (4)	0.124 (6)	−0.010 (3)	0.050 (4)	−0.033 (4)
C14	0.108 (5)	0.070 (4)	0.098 (5)	−0.027 (4)	0.056 (4)	−0.040 (4)
C15	0.102 (4)	0.054 (3)	0.069 (3)	−0.021 (3)	0.031 (3)	−0.013 (3)
C16	0.087 (4)	0.041 (3)	0.061 (3)	−0.001 (3)	0.022 (3)	−0.005 (2)
C21	0.057 (3)	0.054 (3)	0.044 (2)	0.014 (2)	0.007 (2)	0.006 (2)
C22	0.059 (3)	0.056 (3)	0.041 (2)	0.007 (2)	−0.006 (2)	0.008 (2)
C23	0.084 (4)	0.071 (4)	0.044 (3)	0.006 (3)	−0.002 (2)	−0.002 (2)
C24	0.089 (4)	0.080 (4)	0.046 (3)	0.011 (3)	0.015 (3)	0.002 (3)
C25	0.072 (3)	0.074 (4)	0.057 (3)	0.007 (3)	0.019 (3)	0.010 (3)
C26	0.065 (3)	0.057 (3)	0.054 (3)	0.002 (2)	0.008 (2)	0.004 (2)
C31	0.105 (4)	0.067 (4)	0.072 (4)	0.031 (3)	0.010 (3)	0.009 (3)
C32	0.112 (5)	0.090 (5)	0.115 (5)	0.038 (4)	−0.018 (4)	0.033 (4)
C33	0.147 (6)	0.100 (5)	0.067 (4)	0.023 (5)	−0.005 (4)	0.029 (4)
C34	0.159 (7)	0.104 (5)	0.062 (4)	0.049 (5)	0.010 (4)	0.019 (4)
C35	0.095 (4)	0.100 (5)	0.069 (4)	0.033 (4)	0.011 (3)	0.018 (3)

Geometric parameters (Å, º)

Br1—C15	1.888 (6)	C21—C26	1.395 (7)
S1—O2	1.428 (4)	C22—C23	1.386 (6)
S1—O3	1.431 (4)	C23—C24	1.381 (7)
S1—N2	1.616 (4)	C23—H23	0.9300
S1—C22	1.767 (5)	C24—C25	1.366 (8)
O1—C12	1.344 (7)	C24—H24	0.9300
O1—H1A	0.8200	C25—C26	1.380 (7)

N1—C1	1.270 (6)	C25—H25	0.9300
N1—C21	1.413 (6)	C26—H26	0.9300
N2—C35	1.451 (6)	C31—C32	1.489 (8)
N2—C31	1.477 (6)	C31—H31A	0.9700
C1—C11	1.449 (6)	C31—H31B	0.9700
C1—H1	0.9300	C32—C33	1.506 (9)
C11—C16	1.382 (7)	C32—H32A	0.9700
C11—C12	1.413 (7)	C32—H32B	0.9700
C12—C13	1.372 (8)	C33—C34	1.513 (9)
C13—C14	1.368 (10)	C33—H33A	0.9700
C13—H13	0.9300	C33—H33B	0.9700
C14—C15	1.377 (9)	C34—C35	1.464 (8)
C14—H14	0.9300	C34—H34A	0.9700
C15—C16	1.376 (7)	C34—H34B	0.9700
C16—H16	0.9300	C35—H35A	0.9700
C21—C22	1.384 (7)	C35—H35B	0.9700

O2—S1—O3	117.9 (2)	C22—C23—H23	119.8
O2—S1—N2	107.0 (2)	C25—C24—C23	119.6 (5)
O3—S1—N2	111.3 (2)	C25—C24—H24	120.2
O2—S1—C22	109.7 (2)	C23—C24—H24	120.2
O3—S1—C22	107.2 (2)	C24—C25—C26	121.0 (5)
N2—S1—C22	102.8 (2)	C24—C25—H25	119.5
C12—O1—H1A	109.5	C26—C25—H25	119.5
C1—N1—C21	119.7 (4)	C25—C26—C21	119.8 (5)
C35—N2—C31	113.8 (4)	C25—C26—H26	120.1
C35—N2—S1	120.3 (3)	C21—C26—H26	120.1
C31—N2—S1	116.0 (3)	N2—C31—C32	109.6 (5)
N1—C1—C11	121.5 (4)	N2—C31—H31A	109.7
N1—C1—H1	119.2	C32—C31—H31A	109.7
C11—C1—H1	119.2	N2—C31—H31B	109.7
C16—C11—C12	119.6 (4)	C32—C31—H31B	109.7
C16—C11—C1	119.6 (4)	H31A—C31—H31B	108.2
C12—C11—C1	120.7 (5)	C31—C32—C33	111.0 (6)
O1—C12—C13	119.3 (6)	C31—C32—H32A	109.4
O1—C12—C11	122.0 (5)	C33—C32—H32A	109.4
C13—C12—C11	118.7 (6)	C31—C32—H32B	109.4
C14—C13—C12	120.9 (6)	C33—C32—H32B	109.4
C14—C13—H13	119.6	H32A—C32—H32B	108.0
C12—C13—H13	119.6	C32—C33—C34	109.9 (5)
C13—C14—C15	120.9 (5)	C32—C33—H33A	109.7
C13—C14—H14	119.6	C34—C33—H33A	109.7
C15—C14—H14	119.6	C32—C33—H33B	109.7
C16—C15—C14	119.5 (6)	C34—C33—H33B	109.7
C16—C15—Br1	120.9 (5)	H33A—C33—H33B	108.2
C14—C15—Br1	119.6 (4)	C35—C34—C33	111.6 (6)
C15—C16—C11	120.4 (5)	C35—C34—H34A	109.3
C15—C16—H16	119.8	C33—C34—H34A	109.3

C11—C16—H16	119.8	C35—C34—H34B	109.3
C22—C21—C26	119.2 (4)	C33—C34—H34B	109.3
C22—C21—N1	120.8 (4)	H34A—C34—H34B	108.0
C26—C21—N1	120.0 (4)	N2—C35—C34	111.9 (5)
C21—C22—C23	120.0 (4)	N2—C35—H35A	109.2
C21—C22—S1	121.9 (3)	C34—C35—H35A	109.2
C23—C22—S1	118.0 (4)	N2—C35—H35B	109.2
C24—C23—C22	120.4 (5)	C34—C35—H35B	109.2
C24—C23—H23	119.8	H35A—C35—H35B	107.9

O2—S1—N2—C35	30.7 (5)	N1—C21—C22—C23	176.8 (4)
O3—S1—N2—C35	−99.4 (5)	C26—C21—C22—S1	178.2 (3)
C22—S1—N2—C35	146.2 (5)	N1—C21—C22—S1	−4.4 (6)
O2—S1—N2—C31	174.4 (4)	O2—S1—C22—C21	55.2 (4)
O3—S1—N2—C31	44.3 (5)	O3—S1—C22—C21	−175.7 (4)
C22—S1—N2—C31	−70.2 (4)	N2—S1—C22—C21	−58.3 (4)
C21—N1—C1—C11	175.3 (4)	O2—S1—C22—C23	−126.0 (4)
N1—C1—C11—C16	178.2 (4)	O3—S1—C22—C23	3.2 (4)
N1—C1—C11—C12	−3.5 (7)	N2—S1—C22—C23	120.5 (4)
C16—C11—C12—O1	180.0 (5)	C21—C22—C23—C24	−0.1 (7)
C1—C11—C12—O1	1.6 (7)	S1—C22—C23—C24	−179.0 (4)
C16—C11—C12—C13	1.2 (7)	C22—C23—C24—C25	0.9 (8)
C1—C11—C12—C13	−177.1 (5)	C23—C24—C25—C26	−0.9 (8)
O1—C12—C13—C14	179.7 (6)	C24—C25—C26—C21	0.2 (8)
C11—C12—C13—C14	−1.4 (9)	C22—C21—C26—C25	0.6 (7)
C12—C13—C14—C15	0.8 (10)	N1—C21—C26—C25	−176.9 (4)
C13—C14—C15—C16	0.2 (9)	C35—N2—C31—C32	−55.6 (7)
C13—C14—C15—Br1	179.7 (5)	S1—N2—C31—C32	158.4 (5)
C14—C15—C16—C11	−0.4 (8)	N2—C31—C32—C33	56.1 (8)
Br1—C15—C16—C11	−179.9 (4)	C31—C32—C33—C34	−56.3 (9)
C12—C11—C16—C15	−0.2 (7)	C32—C33—C34—C35	54.6 (9)
C1—C11—C16—C15	178.1 (4)	C31—N2—C35—C34	54.9 (7)
C1—N1—C21—C22	135.0 (5)	S1—N2—C35—C34	−160.7 (5)
C1—N1—C21—C26	−47.6 (6)	C33—C34—C35—N2	−53.6 (9)
C26—C21—C22—C23	−0.6 (7)		

Hydrogen-bond geometry (Å, º)

D—H···*A*	*D*—H	H···*A*	*D*···*A*	*D*—H···*A*
O1—H1*A*···N1	0.82	1.86	2.586 (5)	146
C1—H1···O2^{i}	0.93	2.54	3.363 (6)	149
C16—H16···O2^{i}	0.93	2.64	3.461 (6)	147
C23—H23···O3	0.93	2.43	2.846 (7)	107
C25—H25···O3^{ii}	0.93	2.49	3.220 (6)	135
C26—H26···O1^{i}	0.93	2.62	3.467 (7)	151
C35—H35*B*···O2	0.97	2.43	2.852 (7)	106

Symmetry codes: (i) *x*+1/2, *y*, −*z*+1/2; (ii) *x*+1/2, −*y*+1/2, −*z*.